

Molecular dynamics study of T=3 capsid assembly

D.C. Rapaport

Received: Oct 2017 / Accepted:

Abstract Molecular dynamics simulation is used to model the self-assembly of polyhedral shells containing 180 trapezoidal particles that correspond to the T=3 virus capsid. Three kinds of particle, differing only slightly in shape, are used to account for the effect of quasi-equivalence. Bond formation between particles is reversible and an explicit atomistic solvent is included. Under suitable conditions the simulations are able to produce complete shells, with the majority of unused particles remaining as monomers, and practically no other clusters. There are also no incorrectly assembled clusters. The simulations reveal details of intermediate structures along the growth pathway, information that is relevant for interpreting experiment.

Keywords self-assembly · virus · capsid · simulation

PACS 87.16.Ka, 81.16.Fg, 02.70.Ns

1 Introduction

The spontaneous formation of spherical capsids [8,6] that package the genetic payloads of viruses is one of the more fascinating examples of supramolecular self-assembly. Capsid shells, in which icosahedral symmetry is typically a prominent feature, are constructed from multiple copies of one or a small number of different capsomer proteins [1]. This symmetry simplifies the overall structural organization and minimizes the specifications of the construction process, important details since all necessary information must be part of the viral genetic payload.

Experimental methods capable of providing sufficient space and time resolution for direct observation of the intermediate states constituting the assembly pathway have proved elusive until only recently. As a result, knowledge of

Department of Physics, Bar-Ilan University, Ramat-Gan, Israel 52900
E-mail: rapaport@mail.biu.ac.il

the detailed assembly process is limited, even under controlled *in vitro* conditions in which capsomers are able to form complete shells without genetic material [24,3,43]. Justification for focusing on this reduced version of the process stems from the overall robustness of the self-assembly process [5].

An extensive theoretical corpus covering capsid structure and assembly embraces a range of approaches that include thin shells [18], tiling [36], particles embedded on spheres [39], elastic networks [14], stochastic kinetics [13], nucleation theory [40], combinatorics [20], master equations [17], domain decomposition [23], and concentration kinetics [21,12], the last of which is used for interpreting experiment [42,7,15,34] and analyzing reversible growth [41]. There have been numerous simulations of capsid self-assembly using molecular dynamics (MD) [32,27,11,22], and Monte Carlo methods [37,16] that avoid dealing with dynamics; modeling capsid assembly is surveyed in [10]. Experimental ‘analog simulations’ of assembly have been performed using solutions of small plastic particles with adhesive-coated surfaces [2].

The work described in this paper is a continuation of a series of MD simulations modeling capsid self-assembly with rigid particles. The particles are constructed from soft spheres fused together to produce an overall shape tailored to form polyhedral shells, given the appropriate interparticle bonding interactions. The original simulations [32,26] were severely limited by the computational resources available at the time; consequently, the focus was on demonstrating the feasibility of assembly in the absence of solvent, subject to the condition that the bonding process was irreversible, meaning that bonds, once formed, were unbreakable. Shells of size 60 were grown from triangular and trapezoidal particles, the latter corresponding to the structure of a T=1 virus, as well as shells of size 180 resembling the T=3 virus. This was followed by a more computationally demanding study based on reversible assembly, for T=1 shells only, also described in [26]. In the reversible case, bonds are allowed to break when sufficiently stretched. Reversibility is clearly more reasonable from a physical perspective, but since bonds do not typically undergo spontaneous breakage, the approach required that smaller particle clusters be decomposed at regular intervals to avoid kinetic traps due to a depleted monomer concentration.

Inclusion of an atomistic solvent became feasible as a result of further increases in computer performance [27]. The effect of the solvent is to moderate the assembly process, allowing coexisting populations of large clusters and monomers, and eliminating the need to artificially decompose small clusters. However, computational limits restricted the study to the case of triangular particles assembling into 20-particle icosahedral shells. From these simulations it became apparent that assembly involves a sequence of reversible steps, with a high yield of complete shells and a strong preference for minimum-energy intermediates. While ostensibly paradoxical, reversibility is directly responsible for effective assembly due to its ability to discourage particle clusters from becoming trapped in configurations inconsistent with a successful outcome.

Subsequent improvement in computational capabilities led to simulations of larger T=1 shells (size 60) in solution [30]. Increased shell size allows a

broader variety of growth pathways, permitting ‘entropic’ effects to compete more effectively with the energetic considerations that select the pathways of the smaller shells. Comparing the outcomes of growth simulations involving different shell sizes can provide insight into how the size factor influences growth and, in particular, which aspects of growth are common to different shell sizes. In principle, the observed growth pathways and predicted time-dependence of the populations of intermediate structures can be related to behavior that could be measured experimentally [9], and, as experimental technique is refined [19], a search for common structural features becomes feasible.

The present paper describes self-assembly simulations of T=3 shells from trapezoidal particles with reversible bond formation, in the presence of an explicit atomistic solvent, and is the natural extension of earlier work on the smaller (icosahedral and T=1) shells. The model used for the T=1 case, where all trapezoidal particles in the shell occupy equivalent positions, is inadequate for T=3 shells where quasi-equivalence [6,4,33] must be introduced and, as with the earlier irreversible, solvent-free case [26], a simple method for accommodating this effect is employed. Subsequent sections discuss the methodology used for capsomer modeling, simulation and analysis, and describe the results.

2 Methods

MD simulation of large systems over long time periods requires simplified models, avoiding excessive molecular details that would be overwhelming; confirmation of a model’s adequacy, both qualitative and quantitative, must come from outside the simulational framework. Such simplification underlies the choice of molecular representation in the present study of T=3 capsid assembly with an explicit solvent, where the computational needs are much heavier than in the earlier work.

Capsomers are large compact proteins that fit together to form strongly bound closed shells. Design of a simplified model particle for use with MD addresses two prominent generic characteristics of the capsomer, its overall shape and the interparticle bonding forces, while avoiding the complexities associated with specific proteins. Here, the particle that represents a capsomer consists of a set of soft spheres fused together into a rigid structure approximating the shape of a truncated, trapezoidal pyramid (where the interpenetrability of the soft spheres is small relative to the particle size). Attractive forces act selectively between interaction sites embedded in the lateral walls of the particles and are responsible for bonding.

Unlike the earlier T=1 case, where all particles are identical, T=3 shells are more complicated. Real capsomers are able to undergo small conformational changes during assembly, leading to an overall T=3 shell organization referred to as quasi-equivalent. In the simulations, for simplicity, the three distinct shapes (the differences are slight) are assigned to the particles in advance. Figure 1 shows these particles in a fully-bonded trimer configuration.

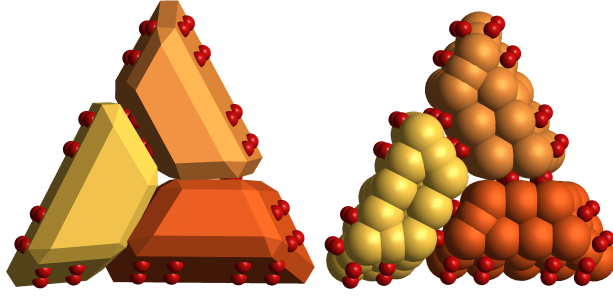


Fig. 1 Bonded trimer showing the effective particle shapes (colors distinguish the three particle types) and the bonding sites (in red), as well as the fused spheres that form each particle.

The particles have relative dimensions and facet angles consistent with the T=3 shell structure. The shell itself is a rhombic triacontahedron [38] with 30 identical faces (see Figure 2 below); each face is subdivided into two isosceles triangles (with base angle 58.283° , so the triangles are almost equilateral), and each of these triangles is divided into three coplanar trapezoids, yielding a total of 180 components. The lateral faces of trapezoids in the same triangle, and faces between triangles of the rhombus, are normal to the triangle plane, while the other lateral faces are inclined at 18° (corresponding to a dihedral angle of 144°). These angles are used in specifying sphere coordinates for the the three kinds of trapezoidal particles used for shell construction.

The excluded-volume interaction between soft spheres on different particles is based on the truncated Lennard-Jones potential

$$u_s(r) = 4\varepsilon [(\sigma/r)^{12} - (\sigma/r)^6] + \varepsilon \quad r < r_c \quad (1)$$

where r is the distance between spheres; a small cutoff range, $r_c = 2^{1/6}\sigma$, ensures that the force is repulsive. This potential is sufficiently stiff to ensure that particle overlap is minimal.

The bonding forces needed for assembly involve quartets of interaction sites on the lateral faces of the particles, shown in Figure 1, and act between corresponding sites on specific face pairs of different particles. The difference between the earlier T=1 case and T=3 is that particle type must now be taken into consideration. The use of several interaction sites per face ensures that particles are correctly positioned and oriented when in a low energy state. The interaction has the form of an inverse power law, gradually changing to a stretched harmonic spring below a small crossover distance,

$$u_a(r) = \begin{cases} e(1/r_a^2 + r^2/r_h^4 - 2/r_h^2) & r < r_h \\ e(1/r_a^2 - 1/r^2) & r_h \leq r < r_a \end{cases} \quad (2)$$

The overall attraction strength is governed by an adjustable parameter e . The range of this force, $r_a = 3\sigma$, is similar to the particle size; the crossover distance is $r_h = 0.3\sigma$, resulting in a narrow harmonic well that limits structural

fluctuations when in a low energy state. While the attraction between sites is not in itself directionally dependent, the involvement of several site pairs enforces particle alignment, further enhancing the rigidity of multiply-bonded structures. A side-effect of the limited structural fluctuations is that the final stages of shell assembly are prolonged, because incoming particles must be correctly aligned for entry into shell openings that leave minimal space for maneuvering.

The particles themselves are immersed in a neutral solvent formed from the same soft-sphere atoms used for the capsomers, a (computationally necessary) simplification replacing the (complex) aqueous medium of reality. A thermostat is included in the solvent dynamics to control temperature [25]. Although an explicit solvent requires significant additional computation, it has several advantages over the implicit (stochastic) alternative. While both are capable of serving as heat baths for energy exchange when bonds form and break, as well as inhibiting the otherwise ballistic particle motion by adding an effective diffusive component ensuring conditions closer to equilibrium, only the explicit approach allows particles that have assembled into structures to offer mutual shielding against disruptive solvent effects, aids cluster breakup without subassemblies needing to collide directly, and incorporates the dynamical correlations of the fluid medium. The choice of solvent representation also affects the actual particle dynamics and can influence the outcome of self-assembly simulations [35].

Typically, relatively large systems and long runs are required to cover the multiple length and time scales intrinsic to the system. A run must follow the evolution in its entirety, from the initial monomeric state until the expected (or unexpected) shells have had the opportunity to self-assemble. Larger shells increase the computation time, as well as requiring more particles to produce enough shells. The size ratio of the particles relative to the solvent atoms is much smaller than in reality, in order to enhance particle mobility; the corresponding mass ratio (here 15) is also reduced. Because of the relatively high mobility and particle concentration the assembly timescales are highly compressed; this is essential to allow the simulation to span the duration of the assembly process, and while this may preclude direct quantitative comparison with experiment, qualitative aspects of the process, both structural and dynamical, ought to be preserved.

Other aspects of the simulations are covered by general MD methodology [25], including the organization of the force evaluations in a manner that scales linearly with the number of particles, dynamics of rigid bodies, stable integration of the equations of motion, boundary conditions and initialization. Results are expressed in reduced (dimensionless) MD units; these are readily converted to physical units (the actual values do not appear in the simulation) for comparison with experiment. The reduced unit of length is expressed in terms of σ (which for argon is 3.4 Å – a typical value), and solvent spheres have unit mass. Energy is expressed in terms of ε , leading to a reduced time unit corresponding to 2.16×10^{-12} s (also for argon); the integration time step is 0.005. Setting $\varepsilon/k_B = 1$ (k_B is the Boltzmann constant) determines the

temperature unit; a fixed temperature of 0.67 is maintained by the thermostat. Additionally, the MD algorithms have been optimized for GPU use [29]. These GPU techniques (that, in many respects, differ significantly from their conventional counterparts) have been extended to handle the specialized needs of the current work, including rigid bodies, multiple particle species, various force types, and have also been updated to utilize new hardware capabilities in more recent generations of GPUs not available for the earlier work (the GPU used here is the NVIDIA K20, whose 2496 computational cores are fully utilized in the simulations).

Numerical snapshots of the particle configurations are recorded at intervals of 2×10^4 time steps during the simulation. Interactive visualization capabilities are incorporated into the simulations allowing progress to be monitored, and also enabling subsequent replay of the recorded snapshot data. The snapshots provide the raw data for offline analysis, primarily the search for assembled structures by means of cluster analysis, as well as for producing imagery such as that included below.

Quantitative cluster analysis is based on an intuitive geometrical definition of bonding, namely, if a pair of trapezoidal particles have all four sets of matching attraction sites within a prescribed range, r_b , they are considered bonded. This is merely a bookkeeping device, since there is nothing special about bond formation given that bonding is reversible (a key factor for successful shell assembly). Once all the bonds have been assigned cluster identification is straightforward [25], since each connected set of bonded particles defines a cluster. Setting $r_b = 0.5$ ($> r_h$) leads to results consistent with direct visualization, namely that structural fluctuations cause minimal spurious bond breakage and there is no false bond designation. Given that the particle design and parameterization ensures that bonded pairs have very limited relative motion, the only permitted cluster in which every particle has a full complement of five bonded neighbors is a closed shell, in the present case having size 180; mutant clusters (whose size would be unbounded) do not develop for the range of e considered here.

3 Results

The total number of particles in the system is $N = 262144$ (64^3), over twice that of [30]. There are $N_p = 8650$ particles, divided among the three species, sufficient for up to 48 complete shells of size 180; the solvent consists of $N - N_p$ atoms, so that the particle fraction is $p = N_p/N = 0.033$. The overall number density is set to 0.1; this determines the volume of the cubic simulation region, and represents a compromise that ensures the solvent influences the motion of the particles without excessively impeding it. The range of the interaction strength parameter e considered here lies between 0.086 and 0.089 where the most interesting results appear. Run length is chosen to maximize growth products within a tolerable computation time; a single run covering 6×10^8 time steps requires ~ 30 days of GPU computation.

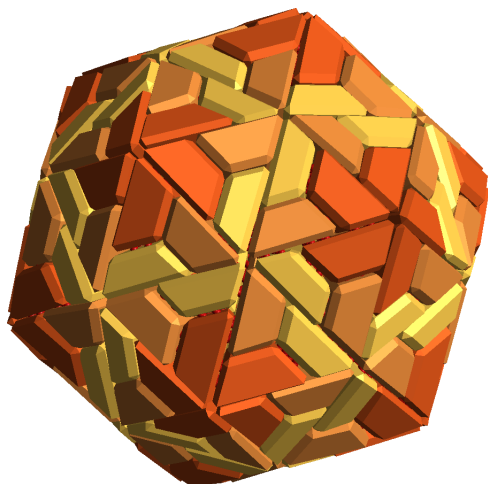


Fig. 2 Single complete shell with 180 particles; colors distinguish the three particle types.



Fig. 3 A picture of the $e = 0.086$ system showing clusters, monomers and solvent near the end of the run, with the space-filling solvent shown semitransparently; because of periodic boundaries some complete shells appear fragmented at opposite faces of the region.

Visualization provides the most comprehensive summary, albeit qualitative, of the outcome of the simulations. Figure 2 shows a closeup of a single complete shell from one of the simulations; the aim is to maximize the yield of such shells.

Figure 3 shows the complete $e = 0.086$ system close to the end of the run, including clusters, monomers and the space-filling solvent; the solvent atoms



Fig. 4 The same $e = 0.086$ system without the solvent.

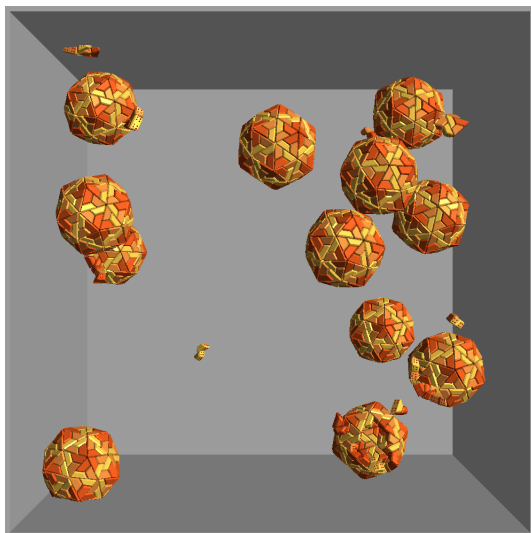


Fig. 5 Another view of the $e = 0.086$ system; both solvent and monomers are omitted allowing the clusters to be seen clearly.

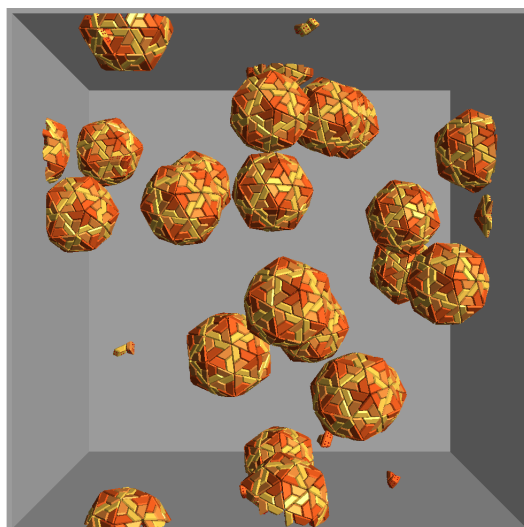


Fig. 6 Clusters at the end of the $e = 0.087$ run.

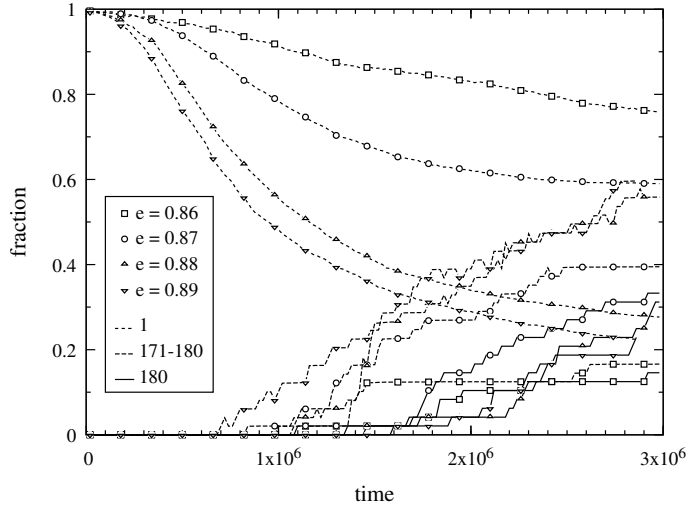
are shown semitransparently to avoid obscuring the interior entirely. The same configuration without the solvent appears in Figure 4. Note that clusters that cross periodic boundaries appear as two or more pieces, a visualization artifact that can be reduced but not completely avoided by translating the system. Another snapshot without the more than 6500 residual monomers (which also hide the interior) is shown in Figure 5; here, seven complete shells can be seen, two clusters with 172 and 178 particles, another three with size > 100 , and a few very small clusters.

Figure 6 shows the cluster configuration at the end of the $e = 0.087$ run. Here there are 16 complete shells (out of a possible 48), two of size 179, one each of sizes 178 and 118, and four of size < 7 ; there are also 5100 monomers.

Cluster analysis, based on the approach described above, complements images of this kind with the quantitative details of shell production, including how the shell yields depend on parameters such as e , and the time-dependent aspects of assembly. The outcomes of the runs considered here are summarized in Table 1 where the final cluster mass fractions, grouped according to size range, are listed. The tabulated results include the monomer fractions, mass fractions of the smallest clusters (range 2–5), intermediate size clusters (two ranges, 6–100 and 101–170), almost complete and complete clusters (> 170), and the complete shells on their own. Subsequent graphs (below) provide a detailed visual breakdown of this information, without recourse to data grouping. The residual monomer fraction is seen to fall with e , whereas the fraction of almost complete and complete clusters increases. Since almost complete clusters (e.g., size > 170) are likely to reach completion eventually, this quantity is probably a more useful measure of e -dependence than the fraction of complete clusters alone, even if the visual impact is reduced. Note

Table 1 Final cluster mass fractions for different interaction strengths e , grouped by cluster size or size range.

e	Time steps ($\times 10^6$)	Cluster mass fraction					
		Size: 1	2–5	6–100	101–170	171–180	180
0.086	600	0.7595	0.0018	0.0015	0.0710	0.1661	0.1457
0.087	600	0.5901	0.0015	0.0000	0.0135	0.3949	0.3329
0.088	600	0.2768	0.0002	0.0088	0.1557	0.5585	0.3121
0.089	570	0.2243	0.0002	0.0055	0.1733	0.5966	0.2289

**Fig. 7** Time-dependent mass fractions of complete shells (180), complete and almost complete shells (171–180) and monomers (1), for different e .

also the intermediate size (101–170) clusters that start to appear at higher e coinciding with falling shell production.

Figure 7 shows how three of the quantities associated with cluster growth vary with time for the different e . The first set of curves shows the gradual appearance of complete shells after an initial lag time. This is accompanied by the diminishing monomer populations shown in the second set of curves. Because the final growth steps tend to occur very slowly, the third set of curves shows the mass fractions of clusters in the size range 171–180; these values, which include the complete shells, are less sensitive to fluctuations over different runs (with the same parameters but with different initial states) and, as suggested previously, are useful for determining the dependence on e since clusters in this size range are likely to form closed shells eventually.

Each shell has a distinct growth pathway through a multitude of possible intermediate subassemblies. Automated tracking of individual clusters is complicated by their mobility in solution and the fact that particles join and leave the cluster in the course of the growth process. Cluster identity is therefore based on comparison with a reference state consisting of the set of structures

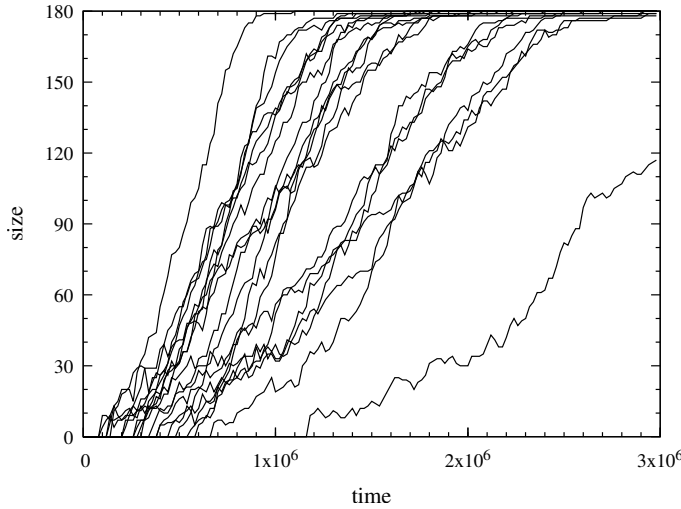


Fig. 8 Graph showing growth of individual clusters, for $e = 0.087$.

in the final configuration, and the cluster with the most member particles in common with the final shell is identified as the precursor of that shell and given its identity. Since growth generally occurs by addition of single particles rather than merging of substantial subassemblies (not impossible, but rarely observed), once a subassembly is large enough to achieve longevity, cluster identification normally yields an unambiguous result consistent with visual monitoring. Problems can occur with very small clusters, but these are of minor interest when considering the overall growth process; examining these small clusters is a separate issue when considering how growth is initiated.

Figure 8 graphs the development of individual clusters for $e = 0.087$, almost all of which grow into complete shells. The different curves show a considerable spread in growth rates and the lack of monotonicity in the curves is evidence that self-assembly pathways are not unidirectional; the spacing of the configurational snapshots determines the temporal resolution. Other particles not in the final shell will also join the cluster temporarily, typically only for short periods, but are excluded from this analysis.

The most detailed quantitative description of how overall cluster growth progresses can be summarized using 3D surface plots showing the time-dependent mass distributions over the full range of sizes, without any grouping. Figure 9 shows such plots for each of the e values considered here. Comparing the graphs reveals the behavioral trend as e is increased, namely a gradual population shift in the final state from monomers to shells, and the absence of intermediate size clusters as the process nears completion. During the period over which most of the growth occurs the size distribution is relatively broad and ill-defined, a consequence of the considerable variation in the growth histories of individual clusters. Signs of late-developing clusters can be seen.

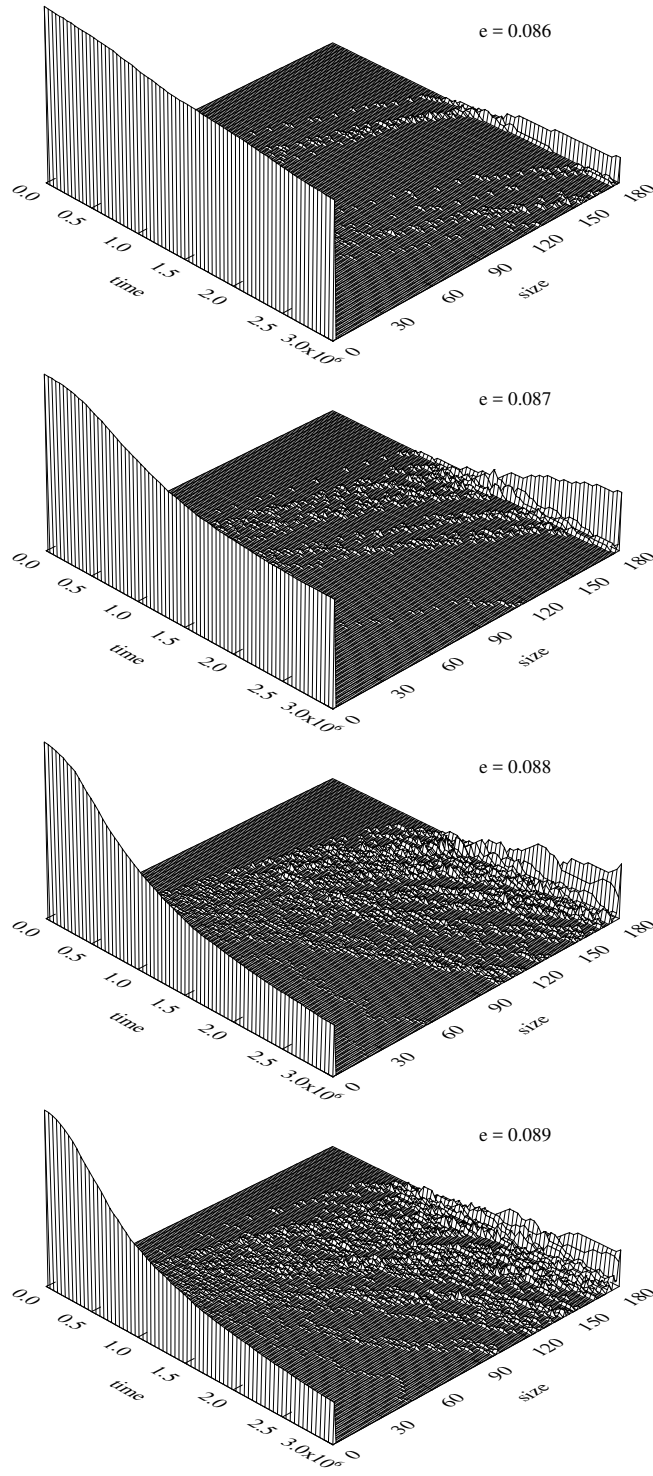


Fig. 9 Time-dependent cluster mass distributions for different e .

For e values below the range discussed here (not shown) the population distribution shifts towards monomers since the assembly process cannot even get started (the stability and lifetimes of dimers and other small clusters were studied for T=1 in [30]). At higher e (also not shown) more subassemblies are able to grow and the competition for monomers reduces their supply below a useful concentration prior to shell completion. Thus there are both fewer monomers and an increased population of almost complete shells, while the number of complete shells is reduced; even though large clusters can release particles back into solution this is usually unhelpful for the growth of other shells given the relative slow monomer diffusion rate. Each of these aspects of the behavior is a consequence of reversible bonding and all are entirely reasonable.

Due to the plethora of intermediate structures there is no unique quantitative characterization useful for specifying pathways that could serve as a ‘reaction coordinate’. Several such measures could be introduced, with varying degrees of meaningfulness, for different stages of assembly, such as the number of holes, hole shapes and sizes, the total length of the boundary surrounding the (one or more) holes, and boundary raggedness. Some are more easily formulated and evaluated than others, but rather than describe such an exercise, a few images of partial shells will be used to illustrate the kinds of intermediate configurations observed. The imagery is augmented by the use of color-coding to convey details of the attachment sequence; this provides a concise visual summary of shell growth history over an extended time interval.

Individual clusters are followed, using the same automated tracking scheme as before, and particles are colored according to when they joined the cluster (or most recently joined if there were multiple events of this kind); the colors span a sliding range covering the previous 5×10^7 time steps in the cluster’s history, starting with red for the most recent additions, through a series of spectral colors, to blue corresponding to additions that occurred either near the start of the range or at an even earlier time. A series of images of this kind, for just a single cluster ($e = 0.087$), appears in Figure 10.

The pictures include examples of the kinds of structural features listed above. There is typically just a single major opening, although several small holes can remain in later growth stages that fill eventually. The nature of the boundary surrounding the particles of the cluster varies in its degree of raggedness. Note that only particles that are present in the final shell are shown; temporarily bonded particles are omitted, although those that return and eventually join the shell are included, with the color coding based on the most recent bonding event. Since each cluster has a different history (best seen when watched as a movie), the rich variety of behavior is evidence of the difficulty in attempting to quantify the finer characteristics of shell growth. Lack of quantification should not, however, prevent the comparison of images of this type with experiment.

It is interesting to note that similar behavior was originally seen for icosahedral shells [27], almost an order of magnitude smaller, as well as for T=1 shells [30,31]. The population distribution is essentially binary, either com-

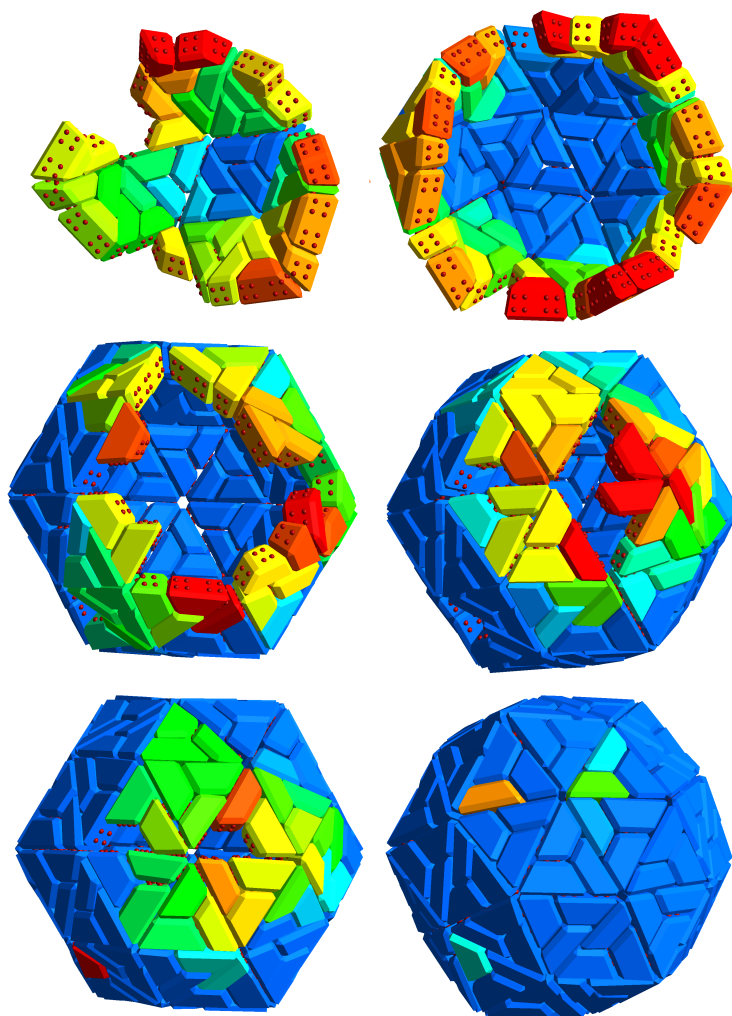


Fig. 10 Color-coded pictures of a single growing cluster; color indicates when particles joined the cluster (relative to the current time, ranging from red for most recent, to blue for earliest).

plete shells or monomers, and even small clusters that might appear to have enhanced stability, particularly the triangle in Figure 1, are absent under conditions favoring optimal growth. There is also the preference for compact structures during early stages of growth followed by clusters with boundaries that are increasingly ragged for larger shell sizes; in the icosahedral case, where a complete classification of all possible intermediates was possible, the clusters were notable for the dominance of (near-)maximally bonded states over a much larger number of possible alternatives.

In the same way that individual shells can grow in different ways, the mean behavior over independent runs can vary. The variation will be prominent during the interval when most of the assembly occurs, as well as in the final shell yields. These are due to two rate-limiting growth stages: First there is the low probability of successfully advancing cluster growth beyond the smallest clusters (e.g., dimers and trimers); the fact that small clusters have a low survival probability means that successfully initiating the growth of an individual shell is a rare event whose consequences affect the entire growth process. Second, the extended duration of the final steps to shell completion due to the difficulty of inserting the final monomers into one or more small holes remaining in the shell. Growth is also retarded because of the serious depletion of the monomer population during assembly. Two T=1 runs for one system size and the corresponding run for a system double the size were compared in [31]. The two smaller systems showed different time-dependent growth, while that of the larger lay in between the two. This demonstrates that the final yield is sensitive to statistical noise and multiple runs would be needed for quantitative studies; these results also suggest that the system size is adequate.

Several other aspects of these self-assembly simulations that were examined in earlier work will be mentioned for completeness; corresponding studies have yet to be carried for T=3 (or even T=1) with solvent, although the observations are likely to remain relevant for the present case. The effect of introducing different particle interface energies to encourage formation of intermediates (typically dimers or trimers) as a precursor to shell growth and its effect on yield and intermediate structures was studied in [26], for T=1 shells without solvent. Closed shells were found to show enhanced stability and breakup was not observed, a consequence of particles being restrained by bonding through all their lateral faces, and the absence of structural fluctuations capable of breaking individual bonds to initiate structural failure. This hysteresis was demonstrated for icosahedral shells [27] by showing that if e was reduced during the run to a level at which assembly would not have occurred, all incomplete assemblies quickly disassembled, leaving only the closed shells.

The appearance of complete shells is confined to a relatively narrow range of attraction strengths e (where raising e over a narrow range is equivalent to reducing temperature); the range is actually so narrow that the high-yield phenomenon could easily have gone unnoticed, sandwiched as it is between the region of no growth and that of many large incomplete clusters. The relevant range depends on the particle concentration $p = N_p/N$ [30], a parameter that governs the frequency of monomer encounters (that oppose solvent-induced cluster breakup); studying this behavior would lead to an e - p phase diagram, a computationally intensive task given the long runs and the need for multiple runs to reduce shell-yield fluctuations. Other parameters yet to be studied systematically include overall density and relative particle mass, as well as design features of the models (such as the choice of interactions, positioning of bonding sites, etc.).

4 Conclusion

Earlier simulational studies of shell growth aimed at modeling *in vitro* viral capsid growth have been extended to the case of 180-particle T=3 shells. Three slightly different particle geometries are used to mimic the effects of quasi-equivalence required for shells with more than 60 elements. In agreement with previous observations, complete shells can be grown if the parameters are correctly chosen, although the computation times required to cover the prolonged growth periods and larger systems are substantially longer.

Maximizing the yield of complete shells was an important goal in formulating the model; the fact that the region size is limited makes this a more prominent issue than it would be *in vivo* where other considerations of a more biological nature are involved. Since allowing bond breakage might be expected to reduce efficiency, the approach used both in the original simulations [32] and as one of the alternatives in [26] (see also [28]) was to make bond formation irreversible (accomplished by altering the form of the pair attraction once inside a suitably defined bonding range, together with a complicated procedure aimed at avoiding bonds incompatible with the final structure). In practice, it turns out that not only is reversible bonding much simpler from a computational point of view (with incompatible bonds managing to break unassisted) but, paradoxically, reversibility is a key contributor to efficient assembly [27, 30, 31]. Indeed, reversibility constitutes a major difference between assembly at microscopic and macroscopic scales, and is a consequence of the thermal ‘noise’ that competes with the forces driving growth, an effect absent at the macroscopic scale.

The author declares that there is no conflict of interest.

References

1. Baker, T.S., Olson, N.H., Fuller, S.D.: Adding the third dimension to virus life cycles: Three-dimensional reconstruction of icosahedral viruses from cryo-electron micrographs. *Microbiol. Mol. Biol. Rev.* **63**, 862 (1999)
2. Breen, T.L., Tien, J., Oliver, S.R.J., Hadzic, T., Whitesides, G.M.: Design and self-assembly of open, regular, 3d mesostructures. *Science* **284**, 948 (1999)
3. Casini, G.L., Graham, D., Heine, D., Garcea, R.L., Wu, D.T.: In vitro papillomavirus capsid assembly analyzed by light scattering. *Virology* **325**, 320 (2004)
4. Casjens, S.: An introduction to virus structure and assembly. In: S. Casjens (ed.) *Virus Structure and Assembly*, p. 1. Jones and Bartlett, Boston (1985)
5. Caspar, D.L.D.: Movement and self-control in protein assemblies: Quasi-equivalence revisited. *Biophys. J.* **32**, 103 (1980)
6. Caspar, D.L.D., Klug, A.: Physical principles in the construction of regular viruses. *Cold Spring Harbor Symp. Quant. Biol.* **27**, 1 (1962)
7. Ceres, P., Zlotnick, A.: Weak protein-protein interactions are sufficient to drive assembly of Hepatitis B virus capsids. *Biochemistry* **41**, 11525 (2002)
8. Crick, F.H.C., Watson, J.D.: The structure of small viruses. *Nature (Lond.)* **177**, 473 (1956)
9. Endres, D., Zlotnick, A.: Model-based analysis of assembly kinetics for virus capsids and other spherical polymers. *Biophys. J.* **83**, 1217 (2002)
10. Hagan, M.F.: Modeling viral capsid assembly. *Adv. Chem. Phys.* **155**, 1 (2014)

11. Hagan, M.F., Chandler, D.: Dynamic pathways for viral capsid assembly. *Biophys. J.* **91**, 42 (2006)
12. Hagan, M.F., Elrad, O.: Understanding the concentration dependence of viral capsid assembly kinetics - the origin of the lag time and identifying the critical nucleus size. *Biophys. J.* **98**, 1065 (2010)
13. Hemberg, M., Yaliraki, S.N., Barahona, M.: Stochastic kinetics of viral capsid assembly based on detailed protein structures. *Biophys. J.* **90**, 3029 (2006)
14. Hicks, S.D., Henley, C.L.: Irreversible growth model for virus capsid assembly. *Phys. Rev. E* **74**, 031912 (2006)
15. Johnson, J.M., Tang, J., Nyame, Y., Willits, D., Young, M.J., Zlotnick, A.: Regulating self-assembly of spherical oligomers. *Nanoletters* **5**, 765 (2005)
16. Johnston, I.G., Louis, A.A., Doye, J.P.K.: Modelling the self-assembly of virus capsids. *J. Phys.: Condens. Matter* **22**, 104101 (2010)
17. Keef, T., Micheletti, C., Twarock, R.: Master equation approach to the assembly of viral capsids. *J. Theor. Biol.* **242**, 713 (2006)
18. Lidmar, J., Mirny, L., Nelson, D.R.: Virus shapes and buckling transitions in spherical shells. *Phys. Rev. E* **68**, 051910 (2003)
19. Medrano, M., Fuertes, M.A., Valbuena, A., Carrillo, P.J.P., Rodríguez-Huete, A., Mateu, M.G.: Imaging and quantitation of a succession of transient intermediates reveal the reversible self-assembly pathway of a simple icosahedral virus capsid. *JACS* **138**, 15385 (2016)
20. Moisan, P., Neeman, H., Zlotnick, A.: Exploring the paths of (virus) assembly. *Biophys. J.* **99**, 1350 (2010)
21. Morozov, A.Y., Bruinsma, R.F., Rudnick, J.: Assembly of viruses and the pseudo-law of mass action. *J. Chem. Phys.* **131**, 155101 (2009)
22. Nguyen, H.D., Reddy, V.S., Brooks III, C.L.: Deciphering the kinetic mechanism of spontaneous self-assembly of icosahedral capsids. *Nano Letters* **7**, 338 (2007)
23. Polles, G., Indelicato, G., Potestio, R., Cermelli, P., Twarock, R., Micheletti, C.: Mechanical and assembly units of viral capsids identified via quasi-rigid domain decomposition. *PLOS Comp. Biol.* **9**, e1003331 (2013)
24. Prevelige, P.E., Thomas, D., King, J.: Nucleation and growth phases in the polymerization of coat and scaffolding subunits into icosahedral procapsid shells. *Biophys. J.* **64**, 824 (1993)
25. Rapaport, D.C.: *The Art of Molecular Dynamics Simulation*, 2nd edn. Cambridge University Press, Cambridge (2004)
26. Rapaport, D.C.: Self-assembly of polyhedral shells: A molecular dynamics study. *Phys. Rev. E* **70**, 051905 (2004)
27. Rapaport, D.C.: Role of reversibility in viral capsid growth: A paradigm for self-assembly. *Phys. Rev. Lett.* **101**, 186101 (2008)
28. Rapaport, D.C.: Modeling capsid self-assembly: design and analysis. *Phys. Biol.* **7**, 045001 (2010)
29. Rapaport, D.C.: Enhanced molecular dynamics performance with a programmable graphics processor. *Computer Phys. Comm.* **182**, 926 (2011)
30. Rapaport, D.C.: Molecular dynamics simulation of reversibly self-assembling shells in solution using trapezoidal particles. *Phys. Rev. E* **86**, 051917 (2012)
31. Rapaport, D.C.: Molecular dynamics simulation: a tool for exploration and discovery using simple models. *J. Phys.: Condens. Matter* **26**, 503104 (2014)
32. Rapaport, D.C., Johnson, J.E., Skolnick, J.: Supramolecular self-assembly: Molecular dynamics modeling of polyhedral shell formation. *Comp. Phys. Comm.* **121**, 231 (1999)
33. Rossmann, M.G., Erickson, J.W.: Structure and assembly of icosahedral shells. In: S. Casjens (ed.) *Virus Structure and Assembly*, p. 30. Jones and Bartlett, Boston (1985)
34. van der Schoot, P., Zandi, R.: Kinetic theory of virus capsid assembly. *Phys. Biol.* **4**, 296 (2007)
35. Spaeth, J.R., Kevrekidis, I.G., Panagiotopoulos, A.Z.: A comparison of implicit- and explicit-solvent simulations of self-assembly in block copolymer and solute systems. *J. Chem. Phys.* **134**, 164902 (2011)
36. Twarock, R.: A tiling approach to virus capsid assembly explaining a structural puzzle in virology. *J. Theor. Biol.* **226**, 477 (2004)

-
37. Wilber, A.W., Doye, J.P.K., Louis, A.A., Noya, E.G., Miller, M.A., Wong, P.: Reversible self-assembly of patchy particles into monodisperse icosahedral clusters. *J. Chem. Phys.* **127**, 085106 (2007)
 38. Williams, R.: *The Geometric Foundation of Natural Structure*. Dover Publications Inc., NY (1979)
 39. Zandi, R., Reguera, D., Bruinsma, R.F., Gelbart, W.M., Rudnick, J.: Origin of icosahedral symmetry in viruses. *Proc. Natl. Acad. Sci. USA* **101**, 15556 (2004)
 40. Zandi, R., van der Schoot, P., Reguera, D., Kegel, W., Reiss, H.: Classical nucleation theory of virus capsids. *Biophys. J.* **90**, 1939 (2006)
 41. Zlotnick, A.: Distinguishing reversible from irreversible virus capsid assembly. *J. Mol. Biol.* **366**, 14 (2007)
 42. Zlotnick, A., Johnson, J.M., Wingfield, P.W., Stahl, S.J., Endres, D.: A theoretical model successfully identifies features of Hepatitis B virus capsid assembly. *Biochemistry* **38**, 14644 (1999)
 43. Zlotnick, A., Mukhopadhyay, S.: Virus assembly, allostery and antivirals. *Trends in Microbiol.* **19**, 14 (2011)